

USC-SIPI REPORT # 158

**Computation of 3-D Velocity Fields
from 3-D Cine CT Images
of a Human Heart ***

by

Samuel M. Song and Richard M. Leahy

June 1990

Signal & Image Processing Institute
Department of Electrical Engineering—Systems
University of Southern California
University Park/MC-0272
Los Angeles, CA 90089

*This work was supported in part by the Hughes Doctoral Fellowship and in part by the Strategic Highway Research Program under Contract No. A002B.

Abstract

The motion of a deforming body is completely characterized by the velocity field (with initial position) generated by the motion. A method of computing the 3-D velocity field from 3-D *cine CTs* of a beating heart is proposed.

Continuum theory provides two constraints on the velocity field generated by a deforming body. Assuming that (1) the image is proportional to some conserved quantity and (2) the imaged medium is incompressible, the velocity field must satisfy the *divergence-free constraint* and the *incompressibility constraint*. Computation of the velocity field using these two constraints is an *ill-posed* problem which may be *regularized* using a smoothness term. We define a penalty function as a weighted sum of the two constraining terms and the smoothness term. Minimization of this function yields the desired velocity field.

Via variational calculus, it can be shown that the solution minimizing the penalty satisfies the Euler-Lagrange equations for this problem. The solution of the Euler-Lagrange equation is a set of coupled elliptic partial differential equations (PDEs). For numerical implementation, the PDEs obtained are discretized resulting in a system of linear equations $\mathbf{Ax} = \mathbf{b}$ where \mathbf{x} is the solution velocity field. The matrix equation is solved using the conjugate gradient algorithm. Examples of experiments using simulated images and a *cine CT* of a beating heart are presented.

Contents

Abstract	i
Contents	ii
List of Figures	iii
1 Introduction	1
2 Constraints on the Velocity Field	3
2.1 Descriptions of Motion of Deformable Media	3
2.2 The Equation of Continuity	4
2.3 The Incompressibility Constraint	5
2.4 The Divergence-Free Constraint	6
3 Problem Description	7
3.1 Formulation	7
3.2 Solution by Minimization of the Penalty $e(s)$	8
3.3 Discretization of the PDE	9
4 Results	11
4.1 Simulated Images	11
4.2 Cine CT of a beating heart	19
5 Summary	21
Acknowledgements	21
Appendix A: The Euler-Lagrange equations for optimizing the penalty function $e(s)$	22
References	24

List of Figures

1	Simulated images for experiments 1, 2 and 3. (a) Experiment 1: Vertically translating circle, time frames 1 and 2. (b) Experiment 2: Diagonally translating circle, time frames 1 and 2. (c) Experiment 3: Deforming ellipse, time frames 1 and 2. The boundary of the outer region is fixed and the motion arises from the inner regions	13
2	Results of experiment 1 with the boundary outlined. The dotted circle shows the inner circle's position in the second frame. (a) Incompressibility constraint only. (b) Incompressibility and divergence-free constraints. . .	14
3	Results of experiment 2 with the boundary outlined. The dotted circle shows the inner circle's position in the second frame. (a) Incompressibility constraint only. (b) Incompressibility and divergence-free constraints. . .	15
4	Results of experiment 3 with the boundary outlined. The dotted ellipse shows the inner ellipse's position in the second frame. (a) Incompressibility constraint only. (b) Incompressibility and divergence-free constraints. . .	16
5	Simulated images for experiment 4: Vertically translating ellipsoid, time frames 1 and 2. The outer ellipsoid is fixed and the inner ellipsoid translates down one voxel.	17
6	Results of experiment 4. 3-D vector field as a function of a 3-D space is projected onto a plane. (a) Incompressibility constraint only. (b) Incompressibility and divergence-free constraints.	18
7	Cine CT of a beating heart overlayed with velocity field vectors. Top: level 4 time 1. Bottom: level 4 time 2.	20

1 Introduction

X-ray computed tomography (CT) is a diagnostic tool for producing cross-sectional images of the human head or body. The reconstructed CT images are proportional to the spatial distribution of the linear x-ray attenuation coefficient within the imaged slice. Since attenuation coefficients vary with tissue type (e.g. blood, muscle, fat, bone), these images yield valuable anatomical information. For most conventional CT scanners the scanning time is on the order of 1 to 10 seconds per slice, consequently, application is limited to parts of the body that are stationary. A modern *cine CT* scanner [1], in which x-rays are produced using an electronically steered electron beam, is able to reduce this scanning time to 50 milliseconds and is therefore ideal for cardiac imaging with minimal motion artifacts. Multiple slices covering the entire heart may be scanned in a few seconds and stored as a sequence of 3D images of the beating heart. This sequence of images may be displayed on a monitor as a movie for qualitative diagnosis based on the motion of the heart. The goal of this paper is to quantify this motion using the data provided by the cine CT. The motion of a beating heart is completely characterized by the velocity field (with initial position) generated by the motion; it is this field that we propose to estimate.

The problem of estimating motion from a sequence of images is often *ill-posed* [2] in the sense of Hadamard [3]. Horn and Schunck [4] reported the first computational algorithm for computing a 2-D velocity field from a sequence of 2-D images using a method commonly referred to as *optical flow*. The ill-posed nature of the problem was overcome via a regularization method of Tikhonov [2]. Several variations on the original optical flow algorithm have since been proposed [5, 6, 7].

The optical flow algorithm of Horn and Schunck [4] computes a velocity vector for every pixel in the image. The *brightness constraint* introduced in [4] is based on the assumption that a ‘point’ in a sequence of images does not change in its gray level from one frame to the next. This brightness constraint alone however does not result in a unique velocity field. By incorporating a regularization or smoothness measure on the velocity field (thus assuming the true field to be spatially smooth) and minimizing a weighted sum of the smoothness term and the error in the brightness constraint, the 2-D velocity field can be computed from a sequence of 2-D images.

Mailloux *et al* [8, 9] have attempted automated motion quantification of a beating heart using echocardiograms. In [8], the optical flow method in [4] was applied directly to 2-D echo images with favorable results. In [9], the velocity field was assumed to be locally linear and the solution constrained to lie on the set of linear vector fields. The linearity constraint, and both the brightness and smoothness constraints of optical flow, can all be shown to be convex. Therefore, by using *projections onto convex sets* (POCS) [10], the velocity field was computed for all components of the linear velocity field: translational, rotational, divergent and shear. One limitation of the results reported by Mailloux *et al* is that they are 2-D approximations of the true 3-D field.

Since the motion of a beating heart is a 3-D phenomena, we formulate and solve the problem directly in 3-D. The formulation is derived from a physical model for the motion

of the imaged medium using continuum theory [11, 12]. In particular, the *equation of continuity* can be applied to all images proportional to the density of some conserved quantity; the incompressibility condition may be applied if the imaged medium is also incompressible.

For a 2-D slice of a 3-D body (e.g. 2-D echocardiograms, or 2-D CT images), the equation of continuity and the incompressibility condition cannot be justified, since in general, and specifically for a beating heart, the motion is not confined to the 2-D slice being imaged and we would expect the above constraints to be violated. For this reason, motion estimation is addressed here as a 3-D problem.

In Section 2 we present a brief review of continuum theory [11, 12] as it applies to 3-D density images. Using this theory, we develop two constraints on the 3-D velocity field generated by a beating heart. With these constraints, the computation of the 3-D velocity field is formulated in Section 3 as an optimization problem and a solution to the optimization problem is developed using the Euler-Lagrange method. The solution is then discretized for computer implementation. Section 4 presents the results for both simulated images and clinical cine CT images of a beating heart.

The presentation to follow introduces and defines a large number of variables. To avoid confusion, these variables are defined below.

$\mathbf{r} = (x, y, z)$: spatial variables or coordinates
$\mathbf{R} = (X, Y, Z)$: material variables or initial position
t	: time
$\mathbf{s}(\mathbf{r}, t) = (u, v, w)$: velocity in Eulerian Description
$\mathbf{S}(\mathbf{R}, t)$: velocity in Lagrangian Description
f	: density image
$D/Dt g$: mobile derivative of g with respect to t
$g_x = \partial g / \partial x$: partial derivative of g with respect to x
$\nabla = (\partial / \partial x, \partial / \partial y, \partial / \partial z)$: gradient operator, spatial
$\nabla \cdot$: divergence operator
(T_x, T_y, T_z)	: spatial extent of the imaging experiment
Ω	$= [0, T_x] \times [0, T_y] \times [0, T_z]$, imaging volume
$\partial\Omega$: surface enclosing Ω
$d\Omega = dx dy dz$: differential volume element
e_S	: cost pertaining to smoothness of $\mathbf{s} = (u, v, w)$
e_I	: cost pertaining to incompressibility constraint
e_D	: cost pertaining to divergence-free constraint
γ_1	: regularization parameter for e_I
γ_2	: regularization parameter for e_D
\mathbf{f}	: discrete version of image f

\mathbf{x} : discrete version of the velocity field $\mathbf{s} = (u, v, w)$

2 Constraints on the Velocity Field

In this section we present two constraints which may be applied to the velocity field of the cine CT of the heart. These constraints are developed within the framework of continuum theory. A fundamental assumption in the following is that the data are *density images* in the sense defined by Fitzpatrick [13], i.e., the images represent some conserved quantity. CT image intensities are proportional to the linear attenuation coefficient. This coefficient is a time-invariant function of the tissue type determined by its chemical composition. It is therefore reasonable to assume that the CT image represents a conserved quantity. A mathematical definition of density images and the conservation property is given in section 2.2. Although the method described here is derived and applied to x-ray CT images, it can be shown that magnetic resonance (MR) images and emission tomographic images are also density images and hence the algorithm described below could also be applied to images collected using these modalities.

2.1 Descriptions of Motion of Deformable Media

Consider a physical body occupying a region $\mathcal{V} \subset \mathbb{R}^3$. This body is in motion and is subject to deformation. The region \mathcal{V} consists of points or particles that can be associated with the position vector $\mathbf{R} = (X, Y, Z)$ in one-to-one correspondence. Therefore the mapping ‘particle $\Rightarrow \mathbf{R}$ ’ is bijective so that each particle is uniquely labeled with a position vector \mathbf{R} .

Let a physical body at time t_0 occupy a region \mathcal{V}_{t_0} and at time t , through motion, occupy a new region \mathcal{V}_t . Then the particle with label $\mathbf{R} = (X, Y, Z) \in \mathcal{V}_{t_0}$ will have moved to a new position $\mathbf{r} = (x, y, z) \in \mathcal{V}_t$. We describe this mapping by

$$\mathbf{r} = \mathbf{r}(\mathbf{R}, t) \tag{1}$$

The mapping $\mathbf{r}(\mathbf{R}, t)$ describes the path of the particle initially located at \mathbf{R} . Therefore, it is natural to define the velocity \mathbf{S} at time t of the particle with label \mathbf{R} as follows.

$$\mathbf{S}(\mathbf{R}, t) = \frac{\partial}{\partial t} \mathbf{r}(\mathbf{R}, t) \tag{2}$$

Further, we assume that the particle with label \mathbf{R} moves to only one \mathbf{r} and conversely, no two particles with different labels arrive at the same \mathbf{r} at the same time. This assumption is the principle of *impenetrability of matter*. Then, the inverse mapping of (1) exists and a pair of invertible mappings are described below.

$$\mathbf{r} = \mathbf{r}(\mathbf{R}, t) \quad \text{and} \quad \mathbf{R} = \mathbf{R}(\mathbf{r}, t) \tag{3}$$

The above pair of invertible mappings depict the transformation between *spatial description* and *material description*. These are also called *Eulerian* and *Lagrangian* descriptions

respectively. In spatial description, the independent variable is \mathbf{r} —the spatial variable. In material description, the independent variable is \mathbf{R} —the material variable. In both cases, t is an independent variable.

In most imaging experiments, pixels or voxels are fixed to a laboratory frame of reference. The motion of the imaged medium is observed with respect to this laboratory frame in which the pixels are fixed. Therefore, the convenient description of motion in most imaging applications seems to be the spatial description. This is the case for the problem of computing the velocity field within the imaging volume. We must express $\mathbf{S}(\mathbf{R}, t)$ in (2) in terms of the spatial variable \mathbf{r} —the pixel coordinates.

Using (3), the velocity may be expressed in terms of the spatial variable \mathbf{r} as below.

$$\mathbf{s}(\mathbf{r}, t) = \mathbf{S}(\mathbf{R}, t) |_{\mathbf{R}=\mathbf{R}(\mathbf{r}, t)} = \mathbf{S}(\mathbf{R}(\mathbf{r}, t), t) \quad (4)$$

This is the spatial description of the particle velocity. In other words, $\mathbf{s}(\mathbf{r}, t)$ is the velocity of the particle passing through the spatial position \mathbf{r} at time t .

2.2 The Equation of Continuity

In this section, we present the *continuity equation* using the conservation of mass. Consider a region \mathcal{V} with a density distribution $f(\mathbf{r}, t)$. Let m be the volume integral of f over \mathcal{V} . If f represents the mass density then m is the total mass in \mathcal{V} . The rate of change in m (within a fixed arbitrary volume \mathcal{V}) is given by

$$\frac{dm}{dt} = - \frac{\partial}{\partial t} \int_{\mathcal{V}} f(\mathbf{r}, t) dV \quad (5)$$

where

dV = differential volume element in \mathcal{V}

This is the change in m as a result of a decrease in density f within \mathcal{V} .

Assuming that f is a density of some conserved quantity—meaning that this quantity is neither created nor destroyed—the change in m above should exactly be matched by the flux of m out of the volume \mathcal{V} . Mathematically,

$$\frac{dm}{dt} = \oint_{\partial\mathcal{V}} f(\mathbf{r}, t) \mathbf{s}(\mathbf{r}, t) \cdot d\mathbf{n} \quad (6)$$

where

$\partial\mathcal{V}$ = surface enclosing \mathcal{V}

$d\mathbf{n}$ = differential normal surface element on $\partial\mathcal{V}$

$\mathbf{s}(\mathbf{r}, t)$ = velocity field in spatial description

Equating (5) and (6) yields the conservation equation which states that the rate of m (the volume integral of density f) leaving an arbitrary region \mathcal{V} must be canceled by the flux of m across the surface $\partial\mathcal{V}$ enclosing that region

$$\frac{\partial}{\partial t} \int_{\mathcal{V}} f dV + \oint_{\partial\mathcal{V}} f \mathbf{s} \cdot d\mathbf{n} = 0 \quad (7)$$

This is the conservation of mass equation (in integral form) that every density image is defined to obey.

Application of the divergence theorem to the flux integral yields

$$\int_{\mathcal{V}} \left(\frac{\partial}{\partial t} f + \nabla \cdot (f \mathbf{s}) \right) dV = 0 \quad (8)$$

This must hold for every arbitrary region \mathcal{V} . Hence, the integrand itself must be identical to zero.

$$f_t + \nabla \cdot (f \mathbf{s}) = 0 \quad (9)$$

This is the conservation of mass equation in differential form. In continuum theory, (9) is referred to as the *equation of continuity*.

Equation (9) may be used as a constraint on the velocity field $\mathbf{s}(\mathbf{r}, t)$. For density images of a compressible medium, the continuity equation (9) may be used as a constraint on velocity field rather than constraints to be discussed in Sections 2.3 and 2.4 to follow. See [14, 15] for example.

2.3 The Incompressibility Constraint

The density f may be expressed in either material or spatial descriptions.

$$\begin{aligned} f^L(\mathbf{R}, t) & \quad \text{in Lagrangian or material description} \\ f^E(\mathbf{r}, t) & \quad \text{in Eulerian or spatial description} \end{aligned}$$

Recall that in material description, the initial position \mathbf{R} is the independent variable whereas in spatial description, \mathbf{r} is independent. In view of (3),

$$f^L(\mathbf{R}, t) = f^E(\mathbf{r}, t) \big|_{\mathbf{r}=\mathbf{r}(\mathbf{R}, t)}$$

Then, by considering the initial position \mathbf{R} as the fixed variable we take the partial derivative of both sides with respect to t . Using $\mathbf{r} = (x, y, z)$,

$$\begin{aligned} \frac{\partial}{\partial t} f^L(\mathbf{R}, t) &= \frac{\partial x}{\partial t} \frac{\partial f^E}{\partial x} \big|_{\mathbf{r}=\mathbf{r}(\mathbf{R}, t)} + \frac{\partial y}{\partial t} \frac{\partial f^E}{\partial y} \big|_{\mathbf{r}=\mathbf{r}(\mathbf{R}, t)} \\ &+ \frac{\partial z}{\partial t} \frac{\partial f^E}{\partial z} \big|_{\mathbf{r}=\mathbf{r}(\mathbf{R}, t)} + \frac{\partial f^E}{\partial t} \big|_{\mathbf{r}=\mathbf{r}(\mathbf{R}, t)} \end{aligned} \quad (10)$$

The partials $\partial x / \partial t$, $\partial y / \partial t$ and $\partial z / \partial t$ evaluated at $\mathbf{r} = \mathbf{r}(\mathbf{R}, t)$ simply represent three components of the velocity in material description $\mathbf{S}(\mathbf{R}, t)$. Using (3) and (4) we may express (10) in spatial description as

$$\begin{aligned} & \frac{\partial}{\partial t} f^L(\mathbf{R}, t) \big|_{\mathbf{R}=\mathbf{R}(\mathbf{r}, t)} \\ &= \frac{\partial f}{\partial t} + u(\mathbf{r}, t) \frac{\partial f}{\partial x} + v(\mathbf{r}, t) \frac{\partial f}{\partial y} + w(\mathbf{r}, t) \frac{\partial f}{\partial z} \end{aligned} \quad (11)$$

where $\mathbf{s}(\mathbf{r}, t) = (u, v, w)$. The superscript E on f have been dropped. From this point on, by f we mean the spatial description of the density— $f^E(\mathbf{r}, t)$. The left hand side of (11) is the rate of change in the density of the particle initially at \mathbf{R} expressed in terms of the spatial variable \mathbf{r} . It is precisely the rate of change of f as seen by an observer moving with the particle initially at \mathbf{R} .

The *convected* or *mobile derivative* is defined as the derivative with respect to time, moving with the particle, as

$$\frac{D}{Dt} = \frac{\partial}{\partial t} + \mathbf{s} \cdot \nabla \quad (12)$$

Then, we may write (11) as

$$\frac{D}{Dt} f = \frac{\partial}{\partial t} f + \mathbf{s} \cdot \nabla f \quad (13)$$

For an incompressible medium, the density f does not change in time if the observation is carried out while moving along with the particle. Therefore $D/Dt f = 0$ if f represents an incompressible medium. This yields the *incompressibility constraint*.

$$f_t + \nabla f \cdot \mathbf{s} = 0 \quad (14)$$

This is equivalent to the *brightness constraint* of optical flow extended to 3-D.

Examples abound where the flow is incompressible and thus satisfying (14). For example, in CT images, the density (and hence CT numbers) of the heart muscle and blood are invariant throughout the systole/diastole cycle. Consequently, cine CT images of the human heart should obey the incompressibility constraint (14).

2.4 The Divergence-Free Constraint

Thus far, the constraints on the velocity field of a moving body represented by a density image were shown to be the continuity constraint (9) and the incompressibility constraint (14). These two constraints may be imposed directly; however, in practice we have found that it was easier to impose the incompressibility constraint and a linear combination of the two constraints.

Equating (9) and (14) yields,

$$\nabla \cdot (f\mathbf{s}) = \nabla f \cdot \mathbf{s}$$

The left hand side can be expanded as $\nabla \cdot (f\mathbf{s}) = f \nabla \cdot \mathbf{s} + \nabla f \cdot \mathbf{s}$, resulting in

$$f \nabla \cdot \mathbf{s} = 0 \quad (15)$$

In continuum theory, (15) is referred to as the *continuity equation for incompressible media*. Equation (15) states that for an incompressible medium the divergence of the velocity field must be zero for regions where f is non-zero. That is,

$$\nabla \cdot \mathbf{s} = 0 \quad (16)$$

This is the *divergence-free* constraint which incompressible density images must obey. For regions where $f = 0$, where it is void of ‘particles’, we also assume the velocity field to be divergence-free for mathematical simplicity.

We end this section by noting that when imposing the divergence-free constraint (16), the incompressibility constraint (14) should also be imposed, since the latter was used in deriving (16).

3 Problem Description

3.1 Formulation

Computation of the velocity field using the incompressibility and the divergence-free constraints is an ill-posed problem, i.e., the solution is not necessarily unique and may be sensitive to small changes in the data.

The cost functional $e_S(s)$ is defined as

$$e_S(s) = \int_{\Omega} (u_x^2 + u_y^2 + u_z^2 + v_x^2 + v_y^2 + v_z^2 + w_x^2 + w_y^2 + w_z^2) d\Omega \quad (17)$$

where

$$\begin{aligned} \Omega &= \{(x, y, z) \in \mathbb{R}^3 : 0 \leq x \leq T_x, 0 \leq y \leq T_y, 0 \leq z \leq T_z\} \\ d\Omega &= dx dy dz \\ \mathbb{R} &= \text{the real line} \end{aligned}$$

and (T_x, T_y, T_z) is the spatial extent of the imaging volume.

Combining the cost e_S (17) and the two constraints, the optimization problem becomes

$$\begin{aligned} &\text{minimize} && e_S(s) \\ &\text{subject to} && f_x u + f_y v + f_z w + f_t = 0 \quad \text{and} \quad u_x + v_y + w_z = 0 \end{aligned} \quad (18)$$

Rather than solving the above optimization problem directly, we consider the equivalent problem.

$$\begin{aligned} &\text{minimize} && e_S(s) \\ &\text{subject to} && e_I(s) = 0 \quad \text{and} \quad e_D(s) = 0 \end{aligned} \quad (19)$$

where

$$\begin{aligned} e_I(s) &= \int_{\Omega} (f_x u + f_y v + f_z w + f_t)^2 d\Omega \\ e_D(s) &= \int_{\Omega} (u_x + v_y + w_z)^2 d\Omega \end{aligned}$$

Since (19) is a convex minimization problem over convex constraints, one could apply the method of Lagrange multipliers to find an optimal solution. However, due to the complexity of the problem and the difficulty in finding the Lagrange multipliers,

we confine our attention to finding an approximate solution to (19) by unconstrained minimization of the penalty function

$$e(s) = e_S(s) + \gamma_1 e_I(s) + \gamma_2 e_D(s) \quad (20)$$

where γ_1 and γ_2 are a pair of real positive constants. We note that an approximate choice of γ_1 and γ_2 is an important theoretical problem; however, we have found in practice that acceptable solutions may be obtained by minimizing $e(s)$ over a fairly wide range of values for γ_1 and γ_2 . By way of justification of this approximate solution, we note that in practice, the data contains noise, and the use of hard constraints as in (18) may result in poor solutions due to the incorporation of the noise into the computed velocity fields. In contrast, the solution obtained by minimizing (20) does not require that the constraints be exactly met, and consequently may be more robust to noise.

In the optical flow formulation of Horn and Schunck [4], a global constraint—a 2-D version of e_S above—was introduced so that a solution may be obtained. The penalty method presented in this section is identical to their approach. In fact, if $\gamma_2 = 0$, our method yields a straight-forward extension of optical flow solution [4] to 3-D.

3.2 Solution by Minimization of the Penalty $e(s)$

In this section, we present a solution minimizing the penalty functional $e(s)$.

$$e(s) = \int_{\Omega} \{ (u_x^2 + u_y^2 + u_z^2 + v_x^2 + v_y^2 + v_z^2 + w_x^2 + w_y^2 + w_z^2) + \gamma_1 (f_x u + f_y v + f_z w + f_t)^2 + \gamma_2 (u_x + v_y + w_z)^2 \} d\Omega \quad (21)$$

where $s = (u, v, w)$ and γ_1 and γ_2 are real positive constants.

Let F be the integrand of (21). Then, from the calculus of variations the solution s_0 must satisfy the following set of Euler-Lagrange equations with either the Dirichlet or the Neumann boundary conditions.

$$\begin{aligned} 0 &= F_u - \frac{\partial}{\partial x} F_{u_x} - \frac{\partial}{\partial y} F_{u_y} - \frac{\partial}{\partial z} F_{u_z} \\ 0 &= F_v - \frac{\partial}{\partial x} F_{v_x} - \frac{\partial}{\partial y} F_{v_y} - \frac{\partial}{\partial z} F_{v_z} \\ 0 &= F_w - \frac{\partial}{\partial x} F_{w_x} - \frac{\partial}{\partial y} F_{w_y} - \frac{\partial}{\partial z} F_{w_z} \end{aligned} \quad (22)$$

The substitution of the partials into the Euler-Lagrange equation (22) results in the following set of partial differential equations (PDEs).

$$\begin{aligned} \nabla^2 u &= \gamma_1 f_x (f_x u + f_y v + f_z w + f_t) - \gamma_2 (u_{xx} + v_{xy} + w_{xz}) \\ \nabla^2 v &= \gamma_1 f_y (f_x u + f_y v + f_z w + f_t) - \gamma_2 (u_{xy} + v_{yy} + w_{yz}) \\ \nabla^2 w &= \gamma_1 f_z (f_x u + f_y v + f_z w + f_t) - \gamma_2 (u_{xz} + v_{yz} + w_{zz}) \end{aligned} \quad (23)$$

where ∇^2 is the Laplacian operator. The solution satisfies equation (23) on the interior of Ω . On the boundary $\partial\Omega$, we impose either the Dirichlet or Neumann boundary conditions (see Appendix A).

If we let $\gamma_2 = 0$, in (23) then the problem is identical to the optical flow problem [4] extended to 3-D; and the solution satisfies the PDEs.

$$\begin{aligned}\nabla^2 u &= \gamma_1 f_x(f_x u + f_y v + f_z w + f_t) \\ \nabla^2 v &= \gamma_1 f_y(f_x u + f_y v + f_z w + f_t) \\ \nabla^2 w &= \gamma_1 f_z(f_x u + f_y v + f_z w + f_t)\end{aligned}\tag{24}$$

As in [4] the Laplacian may be discretized as $\nabla^2 g = \kappa(\bar{g} - g)$ where κ is a constant depending on the differential mask and \bar{g} is the local average of g . Algebraic manipulation and a symbolic inversion of the 3 by 3 matrix result in a Jacobi type iterative algorithm.

$$\begin{aligned}u^{(n+1)} &= \bar{u}^{(n)} - f_x \frac{\bar{u}^{(n)} f_x + \bar{v}^{(n)} f_y + \bar{w}^{(n)} f_z + f_t}{(\kappa/\gamma_1) + f_x^2 + f_y^2 + f_z^2} \\ v^{(n+1)} &= \bar{v}^{(n)} - f_y \frac{\bar{u}^{(n)} f_x + \bar{v}^{(n)} f_y + \bar{w}^{(n)} f_z + f_t}{(\kappa/\gamma_1) + f_x^2 + f_y^2 + f_z^2} \\ w^{(n+1)} &= \bar{w}^{(n)} - f_z \frac{\bar{u}^{(n)} f_x + \bar{v}^{(n)} f_y + \bar{w}^{(n)} f_z + f_t}{(\kappa/\gamma_1) + f_x^2 + f_y^2 + f_z^2}\end{aligned}\tag{25}$$

If the most recent updated values are used in the iteration above, we obtain a Gauss-Seidel iteration. The successive over-relaxation (SOR) method [16] may also be used.

In Jacobi type iterations, convergence is guaranteed if the *row-sum criterion* [16] is met. Unfortunately, the row-sum criterion cannot be checked since the row elements depend on the image f . However, we have implemented (25) in 3-D and obtained convergence for a large class of images. It is more difficult to obtain a Jacobi type iterative formula for the case $\gamma_2 \neq 0$ as this involves a symbolic inversion of a more complex 3 by 3 matrix. Although this symbolic inversion can be done, we chose to use the conjugate gradient algorithm where convergence is guaranteed [17].

3.3 Discretization of the PDE

To compute a solution for the PDEs in (23), the equations must be discretized. Assuming uniform sampling, let the spatial sample grid spacings be Δ_x, Δ_y , and Δ_z for the x, y and z -axis respectively, and let

$$f_{ijk} = f(x, y, z) |_{(x,y,z)=(i\Delta_x, j\Delta_y, k\Delta_z)}, \quad (x, y, z) \in \Omega\tag{26}$$

The partial derivatives (f_x, f_y, f_z, f_t) and the velocity components (u, v, w) are similarly discretized.

Using lexicographical ordering [18], the image samples f_{ijk} can be vector-stacked as $\mathbf{f} = [f_{0,0,0}, \dots, f_{N_x-1, N_y-1, N_z-1}]^T$ where (N_x, N_y, N_z) denotes the discrete

spatial extent of the imaging volume. The vectors, $\mathbf{f}_x, \mathbf{f}_y, \mathbf{f}_z, \mathbf{f}_t$, \mathbf{u} , \mathbf{v} and \mathbf{w} are similarly constructed. The solution vector \mathbf{x} is then defined as

$$\mathbf{x} = \begin{bmatrix} \mathbf{u} \\ \mathbf{v} \\ \mathbf{w} \end{bmatrix} \quad (27)$$

To express the PDEs of (23) in the discrete domain, the matrices below are defined.

$$\begin{aligned} \mathbf{H}_D &= [\mathbf{D}_x \mid \mathbf{D}_y \mid \mathbf{D}_z] \\ \mathbf{H}_I &= [\text{diag}(\mathbf{f}_x) \mid \text{diag}(\mathbf{f}_y) \mid \text{diag}(\mathbf{f}_z)] \\ \mathbf{Q} &= \begin{bmatrix} \mathbf{D}_x^2 + \mathbf{D}_y^2 + \mathbf{D}_z^2 & \mathbf{0} & \mathbf{0} \\ \mathbf{0} & \mathbf{D}_x^2 + \mathbf{D}_y^2 + \mathbf{D}_z^2 & \mathbf{0} \\ \mathbf{0} & \mathbf{0} & \mathbf{D}_x^2 + \mathbf{D}_y^2 + \mathbf{D}_z^2 \end{bmatrix} \\ \text{diag}(\mathbf{f}_x) &= N \times N \text{ diagonal matrix with elements of } \mathbf{f}_x \text{ in the diagonal} \end{aligned} \quad (28)$$

where $\mathbf{D}_x, \mathbf{D}_y$ and \mathbf{D}_z are matrix representations of partial differential operators with respect to x, y and z respectively, and $N = N_x N_y N_z$. With this discretization, (23) has the following discrete form.

$$\mathbf{A}\mathbf{x} = \mathbf{b}, \quad \text{where} \quad \begin{cases} \mathbf{A} = \mathbf{Q} - \gamma_1 \mathbf{H}_I^T \mathbf{H}_I + \gamma_2 \mathbf{H}_D^T \mathbf{H}_D \\ \mathbf{b} = \gamma_1 \mathbf{H}_I^T \mathbf{f}_t \end{cases} \quad (29)$$

Boundary Conditions

Equation (29), is not completely defined without a boundary condition. For example, assuming a central difference scheme, partial differentiation along the z -axis (i.e. \mathbf{D}_z) is not defined at boundaries $z = 0$ and $z = T_z$. A Dirichlet or a Neumann boundary condition (see Appendix A) can be used to define the elements of \mathbf{A} corresponding to the boundary $\partial\Omega$.

If we know the value of s on the boundary $\partial\Omega$, then the natural choice is the Dirichlet boundary condition. In this case, the value of \mathbf{x} , the discrete version of s , is known on $\partial\Omega$. Hence, the matrix equation (29) can be reduced to a smaller dimension discarding the elements corresponding to the boundary $\partial\Omega$. The algorithm only computes elements of \mathbf{x} corresponding to the interior of Ω . Therefore, the differential operators of (29)—assuming the usual central difference derivative, five point Laplacian, etc—are defined everywhere in the interior of Ω and (29) may be solved.

If we have no knowledge of the value of s on the boundary $\partial\Omega$, we insist that the Neumann boundary condition (35) be satisfied. The Neumann boundary condition for our problem becomes

$$\left. \begin{aligned} u_x + \gamma_2(u_x + v_y + w_z) &= 0 \\ v_x + \gamma_2(u_x + v_y + w_z) &= 0 \\ w_x + \gamma_2(u_x + v_y + w_z) &= 0 \end{aligned} \right\} \quad \text{at } x = 0, \text{ and } x = T_x \quad (30)$$

$$\left. \begin{aligned} u_y + \gamma_2(u_x + v_y + w_z) &= 0 \\ v_y + \gamma_2(u_x + v_y + w_z) &= 0 \\ w_y + \gamma_2(u_x + v_y + w_z) &= 0 \end{aligned} \right\} \quad \text{at } y = 0, \text{ and } y = T_y \quad (31)$$

$$\left. \begin{aligned} u_z + \gamma_2(u_x + v_y + w_z) &= 0 \\ v_z + \gamma_2(u_x + v_y + w_z) &= 0 \\ w_z + \gamma_2(u_x + v_y + w_z) &= 0 \end{aligned} \right\} \quad \text{at } z = 0, \text{ and } z = T_z \quad (32)$$

The Neumann boundary condition is not well-defined at edges or vertices of Ω , as the normal vector \mathbf{n} is not continuous there. At an edge we may insist that boundary conditions corresponding to the two intersecting boundary planes both be satisfied; and at a corner, we impose three boundary conditions for the three intersecting boundary planes.

4 Results

In this section, results obtained by the conjugate gradient implementation of the algorithm of the previous section are presented. The 2-D version of the incompressibility constraint—the brightness constraint of optical flow—has been studied extensively; therefore, results obtained (1) with the incompressibility constraint only; and (2) with both incompressibility and divergence-free constraints are compared. It is demonstrated that for density images of moving incompressible objects, using the divergence-free constraint with the incompressibility constraint provides solutions consistent with our intuition of the motion of deforming objects. In all cases presented (except cine CT), the Dirichlet boundary condition was used since at spatial boundaries of the images, the motion was known to be zero. For cine CT of a beating heart, the Dirichlet boundary condition was used for the four boundary planes normal to the x - y plane; and the Neumann boundary condition was used for the remaining planes, i.e., first and last slices of the 3-D image (planes $z = 0$ and $z = N_z - 1$).

4.1 Simulated Images

All simulated images presented in this section were constructed so that the conservation of mass is obeyed. Regions of images were allowed to deform but they were not allowed to change in the area that they occupy in both time frames. Hence, these simulated images clearly satisfies the conservation of mass (7). The incompressibility constraint was imposed on the motion by maintaining a constant gray level for each fixed point of the image as the objects deformed. Thus, the velocity field generated by the simulated images of Figures 1 and 5 were constructed to satisfy the incompressibility and the divergence-free constraints.

2-D images

For illustration purposes, 2-D examples are presented first. Experiment 1 of Figure 1 shows a 64×64 image sequence of a translating circle. The boundary of the outer circle

(of radius 25 pixels) is fixed whereas the inner circle (of radius 13 pixels) translates one pixel down. A physical example of this type of motion is a situation in which the inner region is solid and the outer doughnut is fluid. The images represent the densities of these regions. As the inner circle translates, the outer region (the outer boundary is fixed) experiences motion such that along the left and right regions of the doughnut, upward motion should prevail to evacuate (bottom) and replenish (top) the regions affected by the inner region's motion.

The incompressibility constraint alone does not give results that show such motion. Figure 2 (a) shows the result obtained using only the incompressibility constrain. Here, a general downward motion is shown which does not agree with preceding arguments. When using both constraints, the motion within the doughnut region is seen to accommodate the motion of the inner circle as described above. This is clearly indicated in Figure 2 (b).

Experiment 2 of Figure 1 shows a 64×64 image sequence of a diagonally translating circle. The boundary of the outer circle is fixed as for the first experiment, and the inner circle translates 1 pixel diagonally. Both circles are of the same radius as in the first experiment. Figure 3 illustrate that that the algorithm is not direction sensitive and depicts similar results as in experiment 1.

Experiment 3 of Figure 1 shows a 64×64 image sequence of a deforming ellipse. The outer ellipse (a circle of radius 25) is fixed in both frames and the inner ellipse deforms from a major and minor axis of (13, 10) to (15, 130/15). These numbers were chosen to guarantee the conservation of mass—i.e. the equation of continuity (9). Again, the utility of the divergence-free constraint for density images is clearly illustrated in Figure 4.

These experiments in 2-D clearly indicate the advantage of using the divergence-free constraint for density images.

3-D images

Experiment 4 of Figure 5 shows a $16 \times 16 \times 8$ image sequence of a translating ellipsoid. The outer ellipsoid is fixed in both frames and the inner ellipsoid translates down one voxel. As for the experiments in 2-D, the algorithm was performed with and without the divergence-free constraint. Figure 6 shows the two 3-D vector fields plotted as a function of 3-D space, projected onto a plane. Figure 6 (a)—without the divergence-free constraint—does indicate a general downward motion. However, the motion deep within the inner ellipsoid is significantly smaller than it should be. Figure 6 (b) does not have this undesirable effect due to the divergence-free constraint.

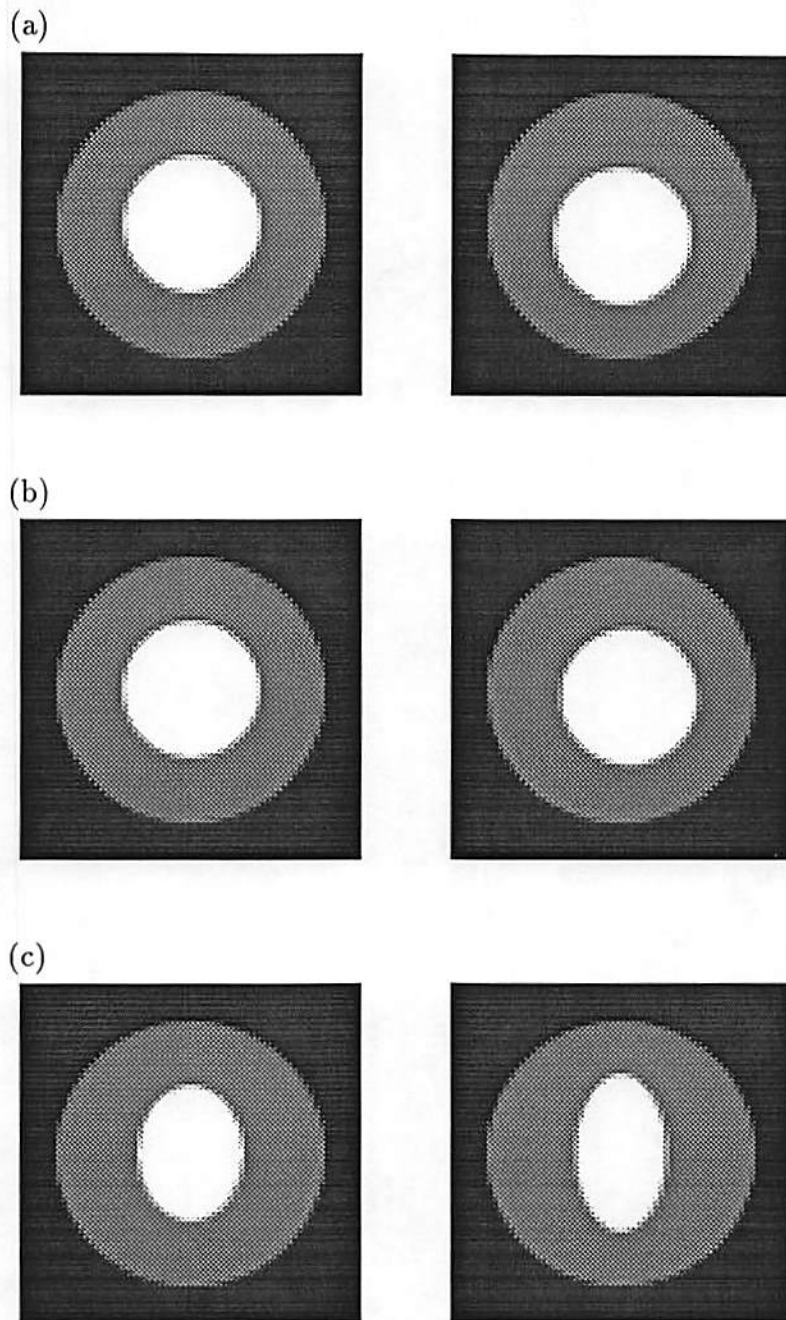


Figure 1: Simulated images for experiments 1, 2 and 3. (a) Experiment 1: Vertically translating circle, time frames 1 and 2. (b) Experiment 2: Diagonally translating circle, time frames 1 and 2. (c) Experiment 3: Deforming ellipse, time frames 1 and 2. The boundary of the outer region is fixed and the motion arises from the inner regions

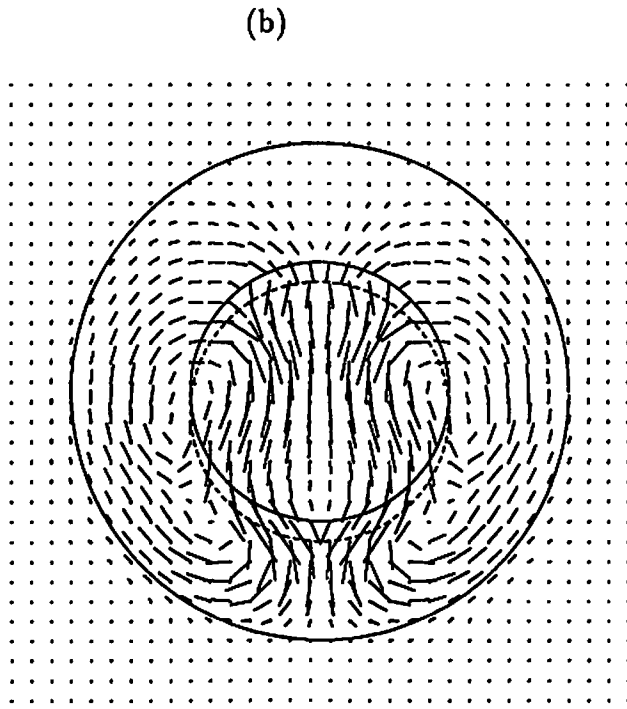
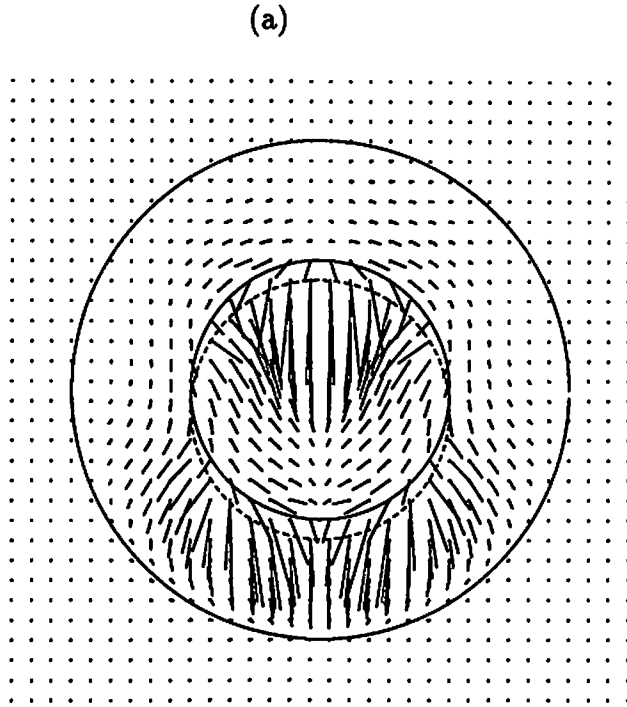
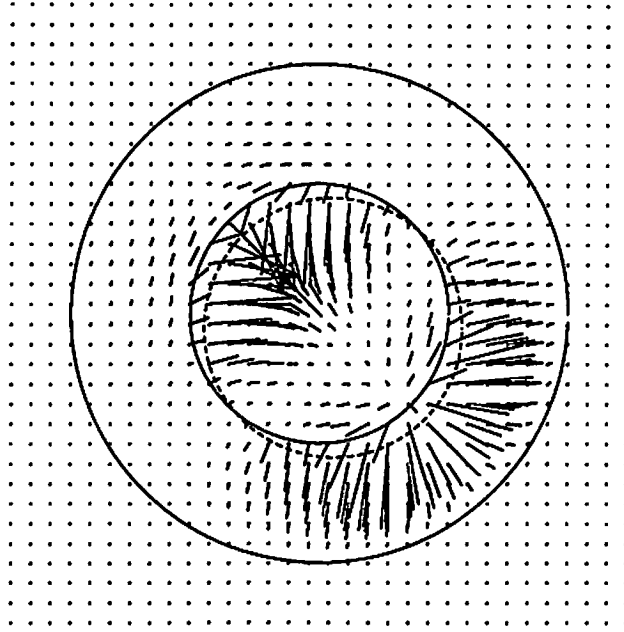


Figure 2: Results of experiment 1 with the boundary outlined. The dotted circle shows the inner circle's position in the second frame. (a) Incompressibility constraint only. (b) Incompressibility and divergence-free constraints.

(a)



(b)

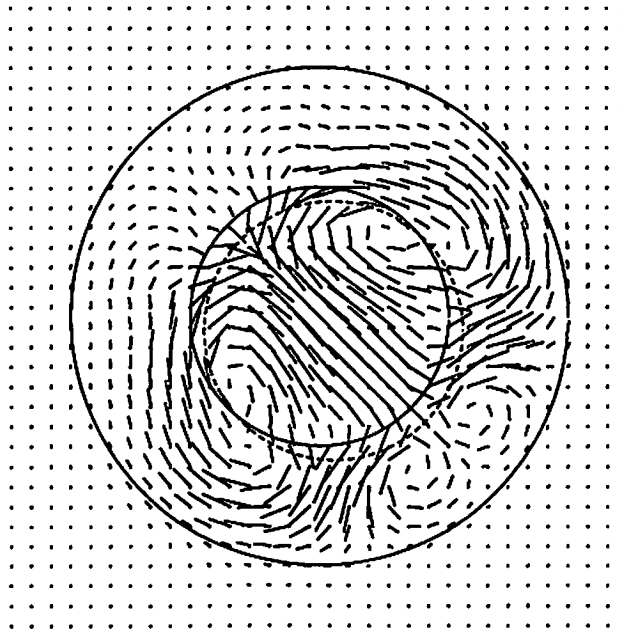
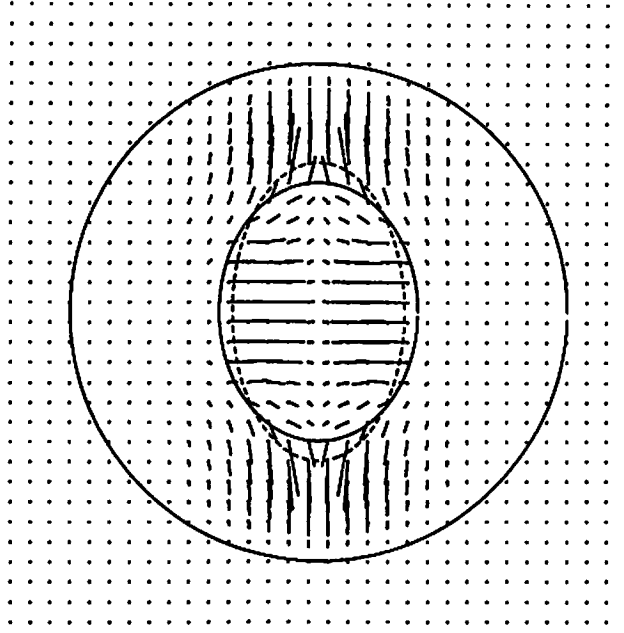


Figure 3: Results of experiment 2 with the boundary outlined. The dotted circle shows the inner circle's position in the second frame. (a) Incompressibility constraint only. (b) Incompressibility and divergence-free constraints.

(a)



(b)

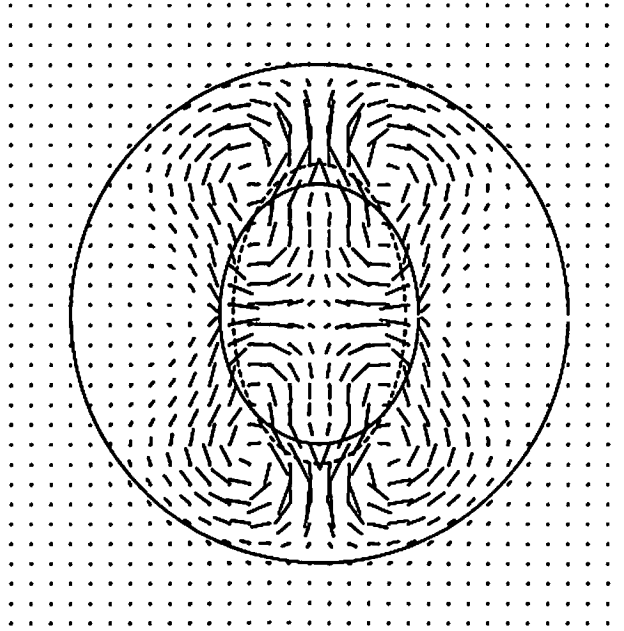


Figure 4: Results of experiment 3 with the boundary outlined. The dotted ellipse shows the inner ellipse's position in the second frame. (a) Incompressibility constraint only. (b) Incompressibility and divergence-free constraints.

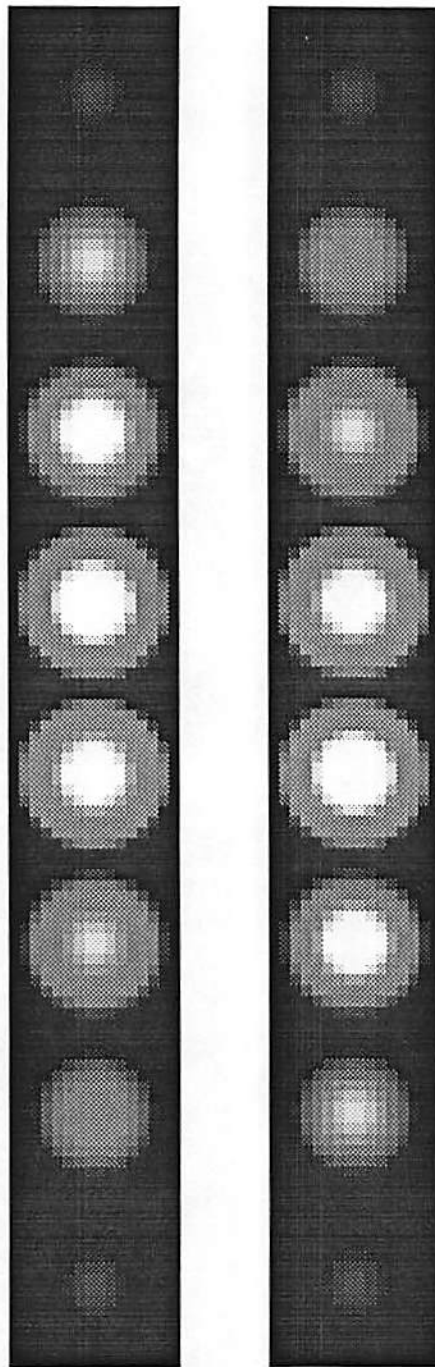


Figure 5: Simulated images for experiment 4: Vertically translating ellipsoid, time frames 1 and 2. The outer ellipsoid is fixed and the inner ellipsoid translates down one voxel.

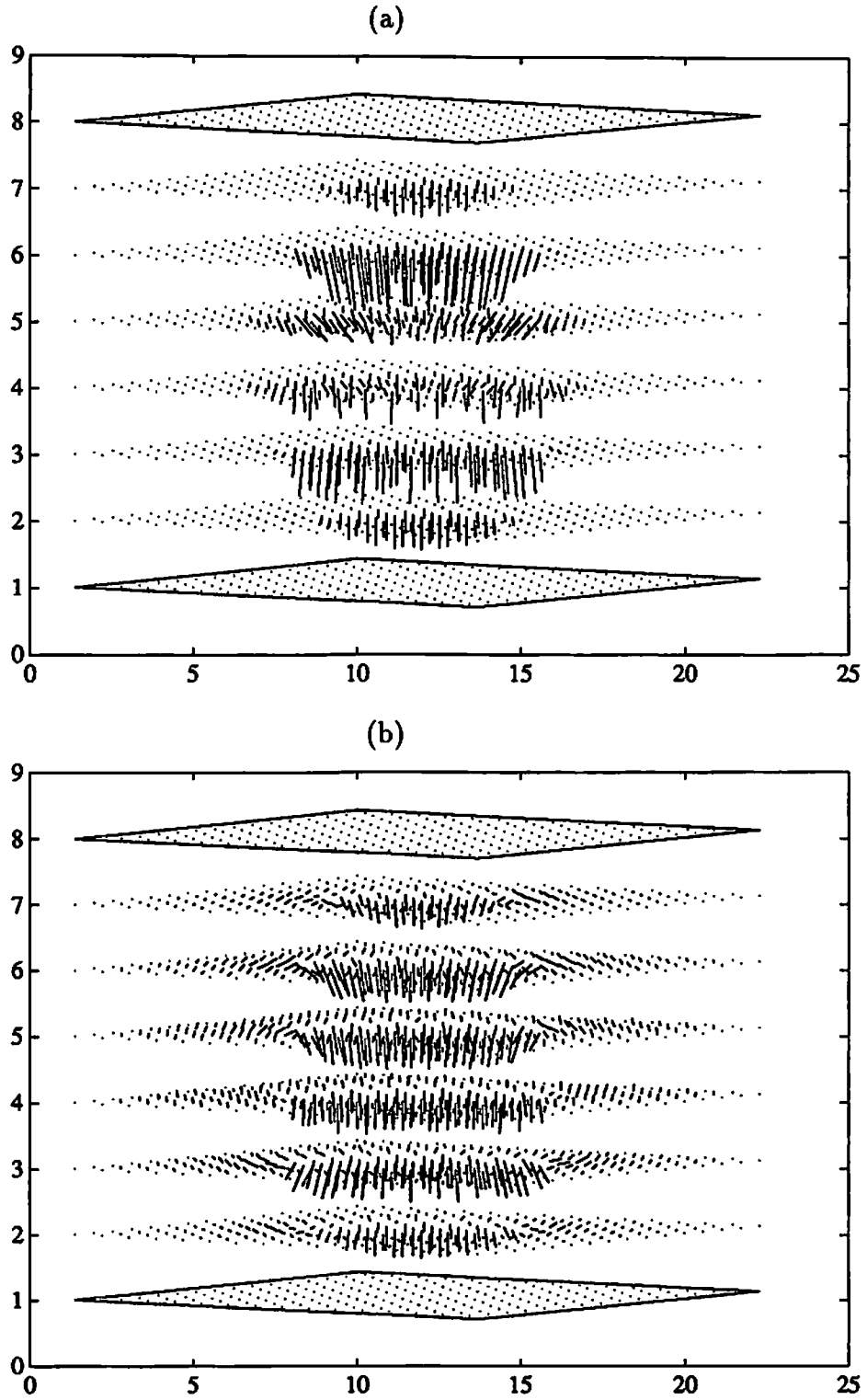


Figure 6: Results of experiment 4. 3-D vector field as a function of a 3-D space is projected onto a plane. (a) Incompressibility constraint only. (b) Incompressibility and divergence-free constraints.

4.2 Cine CT of a beating heart

Images from the Imatron C-100 Ultrafast Scanner [1] were used to evaluate the performance of the algorithm for real data. Low noise in the sequence of cardiac images provided by the Ultrafast Scanner was particularly attractive since the algorithm is based on partial derivatives of the given images. Of 17 consecutive frames of a beating heart, the algorithm was run on the first two frames. Both frames were originally $256 \times 256 \times 8$. These were cut to reduce the computational burden to $128 \times 128 \times 8$ with the heart at the center of the new image. The reduced images were further processed with a simple 2×2 averaging filter (in the x - y plane) to give a pair of $64 \times 64 \times 8$ images. The algorithm was performed on this image.

It is difficult to depict a 3-D velocity field as a function of 3-D space. For a simple motion, such as in experiment 4, the method used in Figure 6 proved useful; however, for complicated motion, these illustrations are difficult to interpret. We present a partial result here by overlaying the velocity vectors onto a plane of the heart image. A complete result can be presented in this manner for any plane desired. Figure 7 shows the fourth slice at time frames 1 and 2 overlayed with the x and y components of the computed velocity.

The motion of the heart in one time frame is small since the Imatron C-100 provides 17 frames per heart beat. Careful examination of both images indicate that the algorithm provides reasonable estimates of the velocity field.

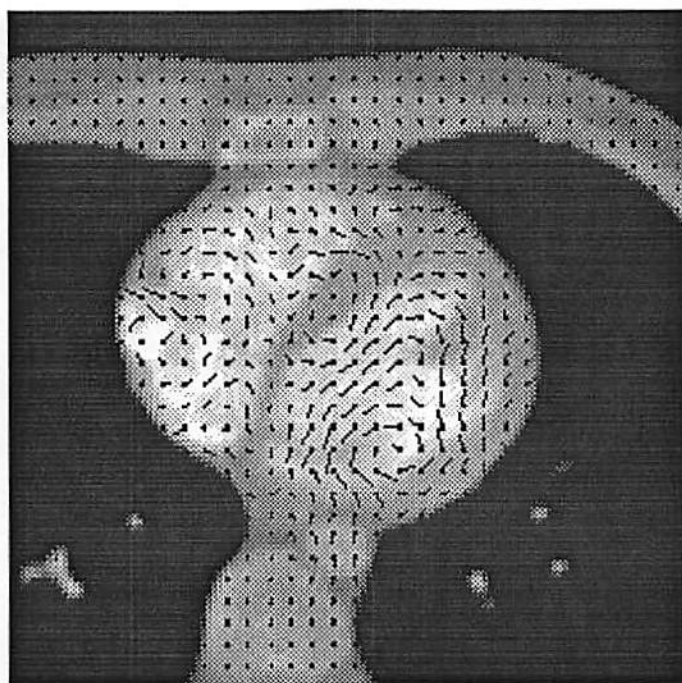
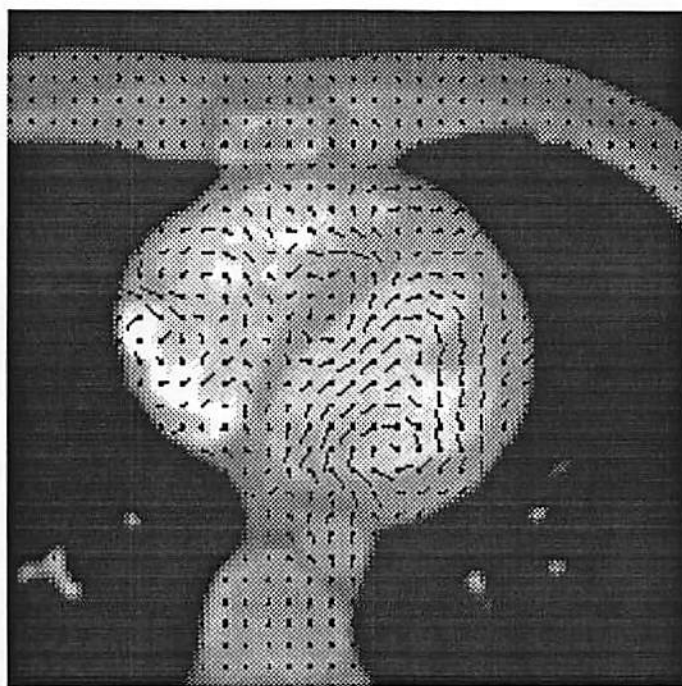


Figure 7: Cine CT of a beating heart overlaid with velocity field vectors. Top: level 4 time 1. Bottom: level 4 time 2.

5 Summary

The goal of this work was to quantify the motion of a beating heart given a cine CT sequence of cardiac images. Since all motion is completely characterized by the velocity field generated by the motion, knowing (or computing) the velocity field completely quantifies the motion. This work was a first attempt at computing the velocity field generated by a cine CT sequence and thus quantifying the motion of a beating heart. However, the algorithm developed also works for other types of images as long as the images are density images of incompressible objects. The algorithm presented in this paper should result in a solution that is agreeable when applied to density images.

We summarize the content of this paper as below.

1. Mathematical relationships of continuum theory was reviewed and successfully utilized as constraints on the velocity field generated by the motion of a deforming body.
2. The problem of computing 3-D velocity field from sequences of 3-D density images was formulated as an optimization problem minimizing a cost functional.
3. The minimization problem was solved by Euler-Lagrange equations resulting in a set of coupled elliptic PDEs.
4. The algorithm was successfully run for simple simulated images and cine CT image of a human heart.
5. The incompressibility constraint is a 3-D version of the well-known brightness constraint of optical flow. The divergence-free constraint introduced in this work is new although a few investigators have alluded to using this constraint in the formulation [13, 19].

Acknowledgements

We would like to thank L. Cox and M. Tokunaga of Imatron Inc. for their general assistance with the Imatron image data. Dr. C. Higgins and Dr. G. Caputo of UCSF Medical Center are gratefully acknowledged for granting permission to use the images in Figure 7. The first author greatly appreciates Dr. D. Boyd of Imatron Inc. for numerous technical discussions on this subject.

Appendix A: The Euler-Lagrange equations for optimizing the penalty function $e(s)$

If g is a Gateaux differentiable functional on a vector space X , a necessary condition [20] for g to achieve an extremum at $s_{ext} \in X$ is that the Gateaux differential

$$\delta g(s_{ext}; h) = 0 \quad \forall h \in X$$

We derive the Euler-Lagrange equations for the functional

$$e(s) = \int_{\Omega} F(s, \partial s) d\Omega$$

where

$$\begin{aligned} s &= (u, v, w) \\ \partial s &= (u_x, u_y, u_z, v_x, v_y, v_z, w_x, w_y, w_z) \\ \Omega &= [0, T_x] \times [0, T_y] \times [0, T_z] \\ d\Omega &= dx dy dz \end{aligned}$$

The problem is set in the space of continuously differentiable vector fields, $C^1(\Omega)$, to ensure the existence of the penalty functional $e(s, \partial s)$, i.e., $s, h = (h_1, h_2, h_3) \in C^1(\Omega)$. By the chain rule of partial differentiation,

$$\begin{aligned} \frac{d}{d\alpha} F(s + \alpha h, \partial(s + \alpha h)) \big|_{\alpha=0} &= F_u h_1 + F_{u_x} h_{1x} + F_{u_y} h_{1y} + F_{u_z} h_{1z} \\ &\quad + F_v h_2 + F_{v_x} h_{2x} + F_{v_y} h_{2y} + F_{v_z} h_{2z} \\ &\quad + F_w h_3 + F_{w_x} h_{3x} + F_{w_y} h_{3y} + F_{w_z} h_{3z} \end{aligned}$$

Therefore,

$$\begin{aligned} \delta e(s; h) &= \int_{\Omega} \frac{d}{d\alpha} F(s + \alpha h, \partial(s + \alpha h)) d\Omega \big|_{\alpha=0} \\ &= \int_{\Omega} (F_u h_1 + F_{u_x} h_{1x} + F_{u_y} h_{1y} + F_{u_z} h_{1z}) d\Omega \\ &\quad + \int_{\Omega} (F_v h_2 + F_{v_x} h_{2x} + F_{v_y} h_{2y} + F_{v_z} h_{2z}) d\Omega \\ &\quad + \int_{\Omega} (F_w h_3 + F_{w_x} h_{3x} + F_{w_y} h_{3y} + F_{w_z} h_{3z}) d\Omega \end{aligned}$$

All three integrals above may be simplified using the divergence theorem of Gauss. For example, we apply the divergence theorem to the first integral.

$$\begin{aligned} &\int_{\Omega} (F_u h_1 + F_{u_x} h_{1x} + F_{u_y} h_{1y} + F_{u_z} h_{1z}) d\Omega \\ &= \int_{\Omega} \left\{ h_1 \left(F_u - \frac{\partial}{\partial x} F_{u_x} - \frac{\partial}{\partial y} F_{u_y} - \frac{\partial}{\partial z} F_{u_z} \right) + \nabla \cdot \begin{bmatrix} h_1 F_{u_x} \\ h_1 F_{u_y} \\ h_1 F_{u_z} \end{bmatrix} \right\} d\Omega \\ &= \int_{\Omega} h_1 \left(F_u - \frac{\partial}{\partial x} F_{u_x} - \frac{\partial}{\partial y} F_{u_y} - \frac{\partial}{\partial z} F_{u_z} \right) d\Omega + \oint_{\partial\Omega} h_1 \begin{bmatrix} F_{u_x} \\ F_{u_y} \\ F_{u_z} \end{bmatrix} \cdot d\mathbf{n} \end{aligned}$$

where

$\partial\Omega$ = surface enclosing Ω

dn = surface normal differential

Similar application of the divergence theorem to the other integrals yield

$$\begin{aligned} \delta e(\mathbf{s}; \mathbf{h}) = & \int_{\Omega} h_1 \left(F_u - \frac{\partial}{\partial x} F_{u_x} - \frac{\partial}{\partial y} F_{u_y} - \frac{\partial}{\partial z} F_{u_z} \right) d\Omega \\ & + \int_{\Omega} h_2 \left(F_v - \frac{\partial}{\partial x} F_{v_x} - \frac{\partial}{\partial y} F_{v_y} - \frac{\partial}{\partial z} F_{v_z} \right) d\Omega \\ & + \int_{\Omega} h_3 \left(F_w - \frac{\partial}{\partial x} F_{w_x} - \frac{\partial}{\partial y} F_{w_y} - \frac{\partial}{\partial z} F_{w_z} \right) d\Omega \\ & + \oint_{\partial\Omega} \left(h_1 \begin{bmatrix} F_{u_x} \\ F_{u_y} \\ F_{u_z} \end{bmatrix} + h_2 \begin{bmatrix} F_{v_x} \\ F_{v_y} \\ F_{v_z} \end{bmatrix} + h_3 \begin{bmatrix} F_{w_x} \\ F_{w_y} \\ F_{w_z} \end{bmatrix} \right) \cdot d\mathbf{n} \end{aligned} \quad (33)$$

We assume for the moment that the last integral above is zero.

The Gateaux differential $\delta e(\mathbf{s}; \mathbf{h})$ must be zero at the extremum \mathbf{s}_{ext} for all $\mathbf{h} = (h_1, h_2, h_3) \in C^1(\Omega)$, it follows that in the first three integrands, the terms inside the parenthesis of the volume integral must be zero and the Euler-Lagrange equations follow.

$$\begin{aligned} 0 &= F_u - \frac{\partial}{\partial x} F_{u_x} - \frac{\partial}{\partial y} F_{u_y} - \frac{\partial}{\partial z} F_{u_z} \\ 0 &= F_v - \frac{\partial}{\partial x} F_{v_x} - \frac{\partial}{\partial y} F_{v_y} - \frac{\partial}{\partial z} F_{v_z} \\ 0 &= F_w - \frac{\partial}{\partial x} F_{w_x} - \frac{\partial}{\partial y} F_{w_y} - \frac{\partial}{\partial z} F_{w_z} \end{aligned} \quad (34)$$

In order for the flux integral in (33) to be zero, which we assumed in deriving the Euler-Lagrange equations above, we impose either Dirichlet or Neumann boundary condition.

Dirichlet boundary conditions give the values of \mathbf{s} on $\partial\Omega$. Therefore, any $\mathbf{h} = (h_1, h_2, h_3)$ in the set of admissible \mathbf{h} must be zero on $\partial\Omega$. Then the flux integrals is zero and the Euler-Lagrange equation follows.

The Neumann boundary condition forces the integrand of the flux integral to zero by imposing the constraint

$$\begin{bmatrix} F_{u_x} \\ F_{u_y} \\ F_{u_z} \end{bmatrix} \cdot d\mathbf{n} = \begin{bmatrix} F_{v_x} \\ F_{v_y} \\ F_{v_z} \end{bmatrix} \cdot d\mathbf{n} = \begin{bmatrix} F_{w_x} \\ F_{w_y} \\ F_{w_z} \end{bmatrix} \cdot d\mathbf{n} = 0, \quad \text{on } \partial\Omega \quad (35)$$

References

- [1] D. P. Boyd and D. W. Farmer, *Cardiac Imaging and Image Processing*, S. M. Collins and D. J. Skorton, eds., ch. 4, pp. 57–87. New York: McGraw-Hill Book Company, 1986.
- [2] A. N. Tikhonov and V. Y. Arsenin, *Solutions of Ill-Posed Problems*. Washington, DC: Winston and Sons, 1977.
- [3] J. Hadamard, *Lecture on the Cauchy Problem in Linear Partial Differential Equations*. New Haven, CT: Yale University Press, 1923.
- [4] B. K. P. Horn and B. G. Schunck, "Determining optical flow," *Artificial Intelligence*, vol. 17, pp. 185–203, 1981.
- [5] W. Enkelmann, "Investigations of multigrid algorithms for the estimation of optical flow fields in image sequences," *Comp. Vision, Graphics and Image Proc.*, vol. 43, pp. 150–177, 1988.
- [6] H. Nagel, "On a constraint equation for the estimation of displacement rates in image sequences," *IEEE Trans. Pattern Anal. Machine Intell.*, vol. 11, no. 1, pp. 13–30, 1989.
- [7] B. G. Schunck, "Image flow: fundamentals and future research," in *Proc. IEEE Conf. Comp. Vision and Patt. Rec.*, vol. CVPR-85, (San Francisco, CA), pp. 560–571, 1985.
- [8] G. E. Mailloux, A. Bleau, M. Bertrand, and R. Petitclerc, "Computer analysis of heart motion from two-dimensional echocardiograms," *IEEE Trans. Biomed. Engr.*, vol. BME-34, no. 5, pp. 356–364, 1987.
- [9] G. E. Mailloux, F. Langlois, P. Simard, and M. Bertrand, "Restoration of the velocity field of the heart from two-dimensional echocardiograms," *IEEE Trans. Med. Imaging*, vol. 8, no. 2, pp. 143–153, 1989.
- [10] D. C. Youla and H. Webb, "Image restoration by the method of convex projections: Part 1: Theory," *IEEE Trans. Med. Imaging*, vol. MI-1, no. 2, pp. 81–94, 1982.
- [11] S. C. Hunter, *Mechanics of Continuous Media*. New York: John Wiley and Sons, 2nd ed., 1983.
- [12] L. A. Segel, "An introduction to continuum theory," in *Modern Modeling of Continuum Phenomena* (R. C. DiPrima, ed.), pp. 1–60, American Mathematical Society, 1986.
- [13] J. M. Fitzpatrick, "The existence of geometrical density-image transformations corresponding to object motion," *Comp. Vision, Graphics and Image Proc.*, vol. 44, pp. 155–174, 1988.

- [14] J. M. Fitzpatrick and C. A. Pedersen, "A method for calculating velocity in time dependent images based on the continuity equation," in *Proc. IEEE Conf. Comp. Vision and Patt. Rec.*, vol. CVPR-85, (San Francisco, CA), pp. 78-81, 1985.
- [15] J. M. Fitzpatrick, "A method for calculating fluid flow in time dependent density images," in *Proc. Electronic Imaging '88*, pp. 347-352, 1988.
- [16] G. D. Smith, *Numerical Solution of Partial Differential Equations: Finite Difference Methods*. Oxford: Oxford University Press, 1983.
- [17] D. G. Luenberger, *Linear and Nonlinear Programming*. Menlo Park, CA: Addison-Wesley, 2nd ed., 1984.
- [18] B. R. Hunt, "The application of constrained least squares estimation to image restoration by digital computer," *IEEE Trans. Computers*, vol. C-22, no. 9, pp. 805-812, 1973.
- [19] P. Y. Simard and G. E. Mailloux, "A projection operator for the restoration of divergence-free vector fields," *IEEE Trans. Pattern Anal. Machine Intell.*, vol. 10, no. 2, pp. 248-256, 1988.
- [20] D. G. Luenberger, *Optimization by Vector Space Methods*. New York: John Wiley, 1969.